Design and performance of a CMOS study sensor for a binary readout electromagnetic calorimeter

J. A. Ballin[a], **R. Coath**[b], **J. P. Crooks**[b], **P. D. Dauncey**[a][*], **A.-M. Magnan**[a], **Y. Mikami**[c][†], **O. D. Miller**[c], **M. Noy**[a][‡], **V. Rajovic**[c][§], **M. Stanitzki**[b], **K. D. Stefanov**[b][¶], **R. Turchetta**[b], **M. Tyndel**[b], **E. G. Villani**[b], **N. K. Watson**[c], **J. A. Wilson**[c], **Z. Zhang**[b]

[a]*Department of Physics, Blackett Laboratory, Imperial College London, London, UK.*
[b]*STFC, Rutherford Appleton Laboratory, Chilton, Didcot, UK.*
[c]*School of Physics and Astronomy, University of Birmingham, Birmingham, UK.*

E-mail: `P.Dauncey@imperial.ac.uk`

ABSTRACT: We present a study of a CMOS test sensor which has been designed, fabricated and characterised to investigate the parameters required for a binary readout electromagnetic calorimeter. The sensors were fabricated with several enhancements in addition to standard CMOS processing. Detailed simulations and experimental results of the performance of the sensor are presented. The sensor and pixels are shown to behave in accordance with expectations and the processing enhancements are found to be essential to achieve the performance required.

KEYWORDS: Calorimeter methods, Detector modelling and simulations, Solid state detectors.

---

[*]Corresponding author

[†]Current address: Institut Pluridisciplinaire Hubert CURIEN, 23 rue du loess - BP28, 67037 Strasbourg CEDEX 2, France.

[‡]Current address: CERN, CH-1211 Genève 23, Switzerland.

[§]Current address: Faculty of Electrical Engineering, University of Belgrade, Bulevar kralja Aleksandra 73, 11120 Belgrade, Serbia.

[¶]Current address: Sentec Ltd, Cambridge, UK.

Contents

1. Introduction

In this paper, we present results from a test sensor which was designed to investigate a novel approach to electromagnetic calorimeters (ECAL). In this approach, the readout of the ECAL is binary, meaning that each channel returns a yes/no result with no further amplitude information. The motivation for such a calorimeter is presented in [1].

Although the potential applications for a binary ECAL are wide, the sensor discussed in this paper was designed to study a specific application, namely the International Linear Collider (ILC) [2]. The work presented in this paper has been done within the context of the CALICE Collaboration [3], which is studying calorimetry for future linear colliders.

In the rest of this paper, the design and fabrication of the test sensor are presented in section 2. Section 3 describes the simulations used for modelling the sensor response. Sections 4 and 5 presents results of individual pixel measurements, from test pixels with analogue readout and bulk pixels with digital readout, respectively. Finally, section 6 describes results of sensor-wide measurements.
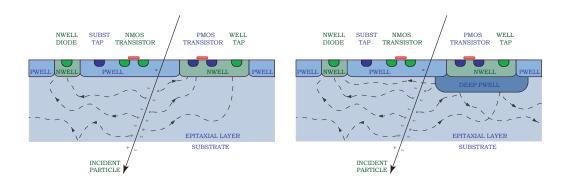
2. Design and fabrication

In this paper, we present results from a test sensor which was designed to investigate a binary ECAL and to demonstrate the feasibility of this approach. Because a complete ECAL for this application would require a total number of pixels of the order of 10^{12}, this development has been named the Tera-Pixel Active Calorimeter (TPAC) sensor. This paper reports on results from the first two versions of a test sensor, TPAC 1.0 and 1.1, which were based on a $0.18\,\mu$m CMOS process.

The use of CMOS structures for light-sensing applications was originally proposed in the 1970s and CMOS imaging sensors were implemented in the 1990s [4]. Numerous recent developments to the pixel design and processing, such as the pinned photodiode, have achieved high-grade performance in areas such as low noise and leakage current. Such performance can be applied beyond the commercial imaging domain, and CMOS sensors have been demonstrated in many alternative applications including particle physics [5].

A key advantage of CMOS imaging is the use of standard CMOS fabrication processes, in which a diverse family of NMOS and PMOS transistors, resistors, capacitors and diodes can be manufactured on the same silicon substrate as the sensitive pixel; hence these sensors are often referred to as Monolithic Active Pixel Sensors (MAPS). In typical imaging applications this allows the integration of the readout electronics and control logic at the edge of the array of imaging pixels, offering a very compact one-chip imaging solution. Although the requirements for particle physics applications of CMOS sensors share many aspects with those for commercial imaging, such as low noise performance, the pixel pitch needed is usually larger. For the binary readout ECAL, pixel sizes of order $100\,\mu$m are needed [1]. This large pixel area provides an opportunity to exploit the full range of components available in the CMOS process, with the possibility to add significant amounts of circuitry inside these larger pixels, rather than around the periphery of the sensor. While these in-pixel components would reduce the light reaching the sensor for imaging applications, they have no effect on the passage of charged particles.

2.1 Process technology

The CMOS silicon substrate comprises a very low resistivity base material, over which a P-doped epitaxial layer is grown, generally up to $20\,\mu$m in thickness. For the application described here, epitaxial layer thicknesses of 5 and $12\,\mu$m were used. The silicon substrate and epitaxial layer are predominantly free of electric fields, so any charge that has been deposited in the silicon will move randomly by diffusion, with typical carrier lifetimes of milliseconds, and will be collected in times of the order of 100 ns (see section 4). A potential barrier exists due to the change in substrate doping between the silicon substrate and the epitaxial layer as well as between the heavily doped P-wells and the epitaxial layer, which is sufficient to keep the majority of carriers within the epitaxial layer. Also an electric field forms around the positively biased N-well to P-epitaxial diode, in which a diffusing electron will be swept towards the N-well and collected as signal. Figure 1 illustrates the basic principles.

Figure 1. *Conceptual illustration of a charged particle crossing a CMOS sensor epitaxial layer. The N-well to P-epitaxial diode at the upper left is the signal collecting diode. The one at the upper right encloses a PMOS transistor which is part of the in-pixel circuitry. Left: the latter is exposed and so can absorb signal charge, reducing efficiency. Right: the N-well diode is shielded from absorbing signal charge by the deep P-well implant between it and the epitaxial layer, reducing signal loss.*

As stated above, the epitaxial layer is the detecting volume where charge is generated. A good approximation is to consider that the most probable total number of electron-hole pairs generated by a MIP in silicon is equal to 80 pairs/μm. For the $12\,\mu$m thick epitaxial layer used in TPAC 1.0, this corresponds to only about 1000 electron-hole pairs. There will also be some contribution to the charge generation from the upper few microns of the substrate which increases the MIP signal charge to around $1200\,e^-$. However, given that the charge can freely diffuse between pixels, the number of charge carriers collected by any single pixel is smaller. Clearly, any further loss, specifically due to charge collection by unrelated N-wells, would make the efficient detection of MIPs in CMOS sensors very difficult, if not impossible.

Due to diffusion, the signal charge will not necessarily be collected by the nearest diode, in which case it continues to diffuse and may be collected by a diode in a neighbouring pixel. In particle physics tracking applications or in imaging sensors this effect is called "crosstalk" and

represents an undesirable loss of image quality for the latter. Although this is less of an issue for an ECAL sensor, it will still degrade the performance in this application and so the pixel design presented in this paper implements four diodes, placed toward the corners of the pixel for optimum crosstalk reduction. The advantage of this approach is also a reduction in charge collection time, as the mean distance to any diode is shorter than the single-diode solution at the same pixel pitch.

The structure of a standard PMOS transistor presents difficulties for use in a pixel design, due to the N-well in which the PMOS device sits. Such N-wells, tied to a positive potential, are as likely to collect diffusing charge as the collecting diode. However, any charge which reaches these N-wells will not be collected as signal on the diode, and so this behaviour represents an inefficiency in charge collection. For this reason, commercial CMOS sensors normally only use NMOS transistors within the pixel, although this significantly limits the circuit functionality that can be implemented. For a complex pixel design with many PMOS transistors and small collecting diodes, this inefficiency could dominate the charge collection and the resulting signal size would be too small to resolve over the electronic noise.

To address the problem of inefficiency caused by PMOS transistors in the pixel, we proposed adding a deep P-well implant to the standard CMOS process. This high-energy implant creates a heavily P-doped beneath the N-well of a PMOS transistor, as shown in figure 1. The potential barrier that forms, much like the boundary between the epitaxial layer and the substrate, is again sufficient to keep the majority of carriers within the epitaxial layer, and more importantly, from being collected by the N-well. This technique restores the charge collection efficiency of the sensor to be close to 100%, although some minor reduction in the initial signal charge will occur, as charge deposited in the small proportion of the epitaxial layer that is now occupied by the deep P-well implant will be lost.

For the successful implementation of this project, the deep P-well module was implemented in a leading $0.18\,\mu$m commercial process. This fabrication process is called "Isolated N-well MAPS" (INMAPS) and is described in detail elsewhere [6]. The INMAPS process features up to six metal layers, precision passive components for analogue circuit design, and may be stitched to manufacture sensors up to wafer scale. Whilst for this project a particular commercial partner was selected, the technology could be implemented in many modern CMOS processes. This is an important feature if large-scale production were ever required for a full-size calorimeter.

The TPAC sensors were manufactured using the INMAPS process, and implemented deep P-well implants in the pixels to achieve a high charge collection efficiency. To further understand the device physics, the same design was manufactured with two thicknesses ($5\,\mu$m or $12\,\mu$m) of the epitaxial layer and with or without the deep P-well implant.
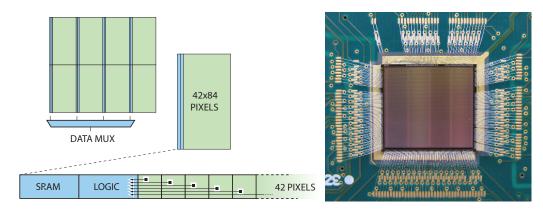
2.2 Overall architecture

The TPAC sensors comprise a 168×168 pixel array, totalling 28,224 pixels, together with row control logic, on-sensor SRAM memory banks and I/O circuitry in a $9.7 \times 10.5\,$mm^2 die. The sensor has been developed with the ILC application in mind. It is designed to be sensitive during a "bunch train", a short period of the order of 1 ms, which is subdivided into "bunch crossings", typically with several thousand bunch crossings per train. This structure is consistent with the proposed ILC operation. The sensors collect the charge deposited by an incident particle in pixels arranged on a $50\,\mu$m pitch. This signal is compared with a global threshold and if above threshold,

the bunch crossing time-code and location of the pixel "hit" is recorded in on-sensor memory for readout following the bunch train.

Four different pixel designs have been implemented for evaluation, which fall into two distinct architectures, called pre-shape and pre-sample. These four designs are arranged in four quadrants of 84×84 pixels. All pixels contain four small N-well diodes for charge collection and these are identical for all four designs. Pixels may be individually masked, allowing any permutation of single pixels to be operated and evaluated.

A common control and readout architecture serves all pixel varieties, allowing the sensor to be operated as a whole or as sub-regions. Rows of 42 pixels share row control logic and SRAM memory, while columns of 168 such rows form a region which shares data readout. All four regions multiplex their data for external readout off-sensor. An overview of the architecture is shown in figure 2, together with a photograph of the TPAC 1.0 sensor.

Figure 2. *Left: overview of sensor architecture; see text for a detailed explanation. Right: photograph of the sensor mounted on its PCB. The four pixel regions and memory areas are visible within the central area of the sensor.*

2.3 Pre-shape pixel

The pre-shape pixel is based on a conventional analogue front end for a charge-collecting detector and is shown in figure 3.

Four diodes are connected to a charge preamplifier, which generates a voltage step output in proportion to the collected charge. A CR-RC shaper circuit with an overall peaking time of around $150\,\text{ns}$ generates a pulse output in proportion to the input signal. Including the further circuit gain, full circuit simulation predicts a gain of $164\,\mu\text{V}/e^-$ with respect to total input charge. The simulated response of the charge preamplifier to signals of varying magnitude is shown in figure 4. This signal, along with a local common-mode reference, form the pseudo-differential inputs to the two-stage comparator.

Following a charge deposit, the shaper circuit returns to a stable state after a time depending on the signal size, and is then able to respond to another input deposit. Saturation in the shaper circuit occurs for signal charge deposits greater than $2500\,e^-$, beyond which the shaper output becomes non-linear and takes a longer time to return to the steady state. Non-recoverable saturation of the pixel occurs when the preamplifier stage has integrated $10\,\text{k}e^-$ on the diode node, beyond which
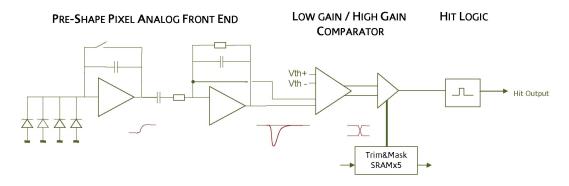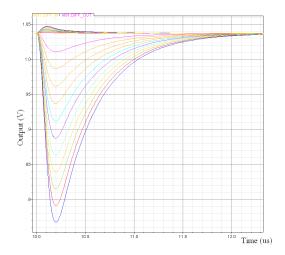
Figure 3. *Pre-shape pixel circuit; see text for a detailed explanation.*

Figure 4. *Simulated pre-shape pixel circuit response as a function of time, for signals injected at the preamplifier input at a time corresponding to 10 μs on the time axis. The circuit response at the comparator input is shown. The input signals shown have various magnitudes up to a maximum of 2500 e⁻, in steps of 250 e⁻. The input signal shape is modelled as an exponential rise with a 50 ns time constant. Together with the finite preamplifier response speed, this means the observed signals peak around 200 ns after the signal injection time.*

the gain of the pixel deteriorates, reaching 50% after $22\,\mathrm{k}e^-$, until it will no longer respond to an input signal. The preamplifier reset is used to initialise the pixel before the start of a bunch train. The expected incident signal charge for a single pixel during a bunch train for the ILC ECAL application is small compared to these saturation limits.

To achieve high circuit gain in the preamplifier, a small value of the feedback capacitance was required, which was made using two larger capacitors in series to comply with manufacturing design rules. Two different simulation tools, Eldo [7] and Spectre [8], were used to evaluate the optimum orientation of the series feedback capacitors, but the two tools selected different topologies for highest gain. Two capacitor orientations were therefore implemented on the TPAC 1.0 sensor as subtle variants of the pre-shape pixel and these occupy quadrants 0 and 1. Results from and comparisons of the performance of both quadrants 0 and 1 are shown in the following sections.

The in-pixel comparator has two stages. The first stage takes two differential signals, and produces a real-time differential result, with some small analogue signal gain. The second, high-gain comparator generates the full-swing discriminator output, and applies an offset trim adjustment with a four-bit resolution. The output of the second comparator is enabled with a one-bit mask which can be used to prevent the pixel from generating hit outputs.
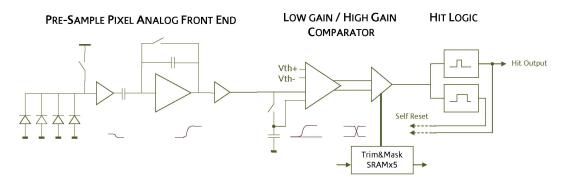
Pixels which go above threshold generate a fixed length pulse using a monostable circuit, the output of which is connected to row control logic outside the pixel. The length of the resulting hit output pulse is thus independent of the signal size.

Electronic circuit noise is estimated at the input to the differential comparator and referred back to the diode node using the charge gain. The dominant noise source is the input transistor of the preamplifier circuit; the predicted equivalent noise charge (ENC) for this pixel is $23\,e^-$.

The nominal power consumption for the pre-shape pixel is $8.9\,\mu$W during operation, although the circuit would be powered off between bunch trains at the ILC. Assuming a factor of 100 reduction in power by this method, this is equivalent to an average power consumption of $36\,\mu$W/mm^2 and hence is is significantly larger than the target power of the analogue ECAL designs for the ILC detectors [9, 10]. However, the main aim of the TPAC 1.0 sensor is to investigate the concept of a binary ECAL and demonstrate the feasibility of the design with a new technology. Power was regarded as a secondary issue, at least for this first demonstrator. Lower power designs will be considered in future versions of the sensor.

2.4 Pre-sample pixel

The pre-sample pixel architecture is closer to that of a conventional MAPS optical sensor. It has in-pixel analogue storage of a reference level, and is shown in figure 5. This design was found to perform worse than the pre-shape circuit in initial tests and testing was stopped early on to concentrate on the latter. Only pre-shape pixels were implemented in the next version of the sensor. Hence although no detailed study of its performance was done, and hence no pre-sample results are shown in the rest of this paper, the design is described here for completeness.
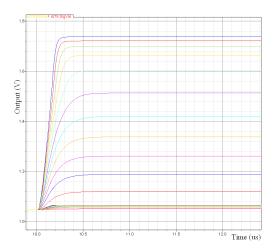

Figure 5. *Pre-sample pixel circuit; see text for a detailed explanation.*

The pixel diodes are reset and the reset level is sampled and stored in-pixel prior to the start of each bunch train. Charge integrates on the four collecting diodes, causing a small voltage step proportional to the collected charge and the node capacitance. A charge preamplifier provides a

voltage step which, along with the local sample of the reset level, forms a pseudo-differential input to the same two-stage comparator as for the pre-shape design. The predicted gain of the circuit is $440 \, \mu\text{V}/e^-$. The charge amplifier and reference sample must be reset after a hit before the pixel can detect another hit; this is undertaken by the in-pixel logic.

The simulated response of the circuit to signals of varying magnitude is shown in figure 6. Saturation in the pre-sample pixel occurs when the diode node has integrated $64 \, \text{k}e^-$, beyond which non-linear operation is expected.

Figure 6. *Simulated pre-sample pixel circuit response as a function of time to input signals injected at a time corresponding to 10 μs on the time axis. The input signals shown have various magnitudes up to a maximum of 2500 e^-, in steps of 250 e^-. The input signal shape is modelled as an exponential rise with a 50 ns time constant.*

Similarly to the pre-shape pixel, a small capacitance in the preamplifier feedback is made with two capacitors in series. This gives rise to two subtle variants of the pre-sample pixel, again based on results from different simulator tools, and these occupy quadrants 2 and 3.
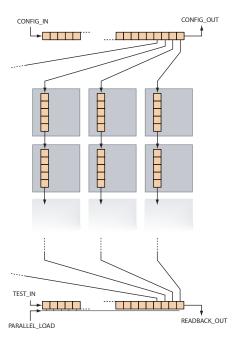
The in-pixel comparator stage is common to all pixel architectures, but the pre-sample pixel includes an additional monostable circuit to generate the self-reset signals that are necessary to reset the amplifier and the reference sample in preparation for another input signal.

Electronic circuit noise is estimated at the input to the differential comparator and referred back to the diode node using the charge gain. The circuit simulation predicts an ENC at this input of $22 \, e^-$. The dominant noise sources are the input transistor of the first source follower buffer and the input device in the charge amplifier circuit. However, the overall observed noise when operating the pixel will be larger by an additional factor of $\sqrt{2}$ to account for the uncorrelated sampling nature of this pixel. This correction needs to be applied to the real-time simulation noise level and so predicts an overall noise of $37 \, e^-$.

The nominal power consumption for the pre-sample pixel is $9.3 \, \mu\text{W}$ during operation, although again the circuit would be powered off between bunch trains at the ILC.
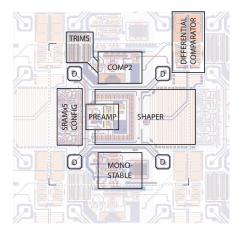
2.5 Mask and trim configuration

Each pixel contains a five-bit SRAM shift register, which is used to store a per-pixel trim (four bits) and a mask flag (one bit). The configuration shift registers are not used while the sensor is in active operation, but these configuration data are programmed during sensor initialisation, and are held indefinitely in each pixel until the sensor is powered down or the data are rewritten. The configuration data are loaded through a serial interface, which shifts single-bit data into each of 168 columns simultaneously, as illustrated in figure 7. Serial data outputs are available at two points to enable data read-back for error-rate monitoring. The data read is destructive, so in normal operation the read-back occurs after hits have been collected. The total configuration memory space on the sensor is 138 kbits.
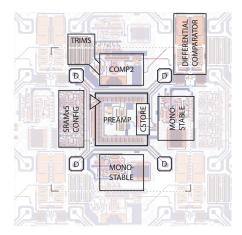

Figure 7. *Overview of logic for configuration data write and readback. To load, one bit of the configuration data for each column are shifted into the register at the top of the diagram. When completed, these bits are parallel-loaded into the pixels below. This is continued until all pixel bits are loaded. The previously stored configuration data are captured in the register at the bottom of the diagram and read out, allowing a consistency check.*
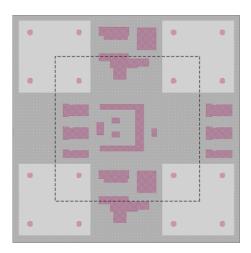
2.6 Pixel layout

The pre-shape and pre-sample pixel layouts are illustrated in figure 8. The pre-shape pixel comprises 160 transistors, 27 capacitor cells and a large polysilicon resistor. The pre-sample pixel comprises 189 transistors and 34 capacitor cells. The two pixel architectures use the same diode positions. The diodes are not located exactly on a 25 μm pitch square grid but were moved slightly towards the corners of the 50 μm pixel. These positions were optimised for charge collection using the simulation described in section 3.1.
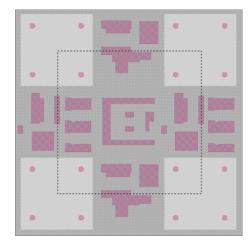
Figure 8. *Pixel layouts; pre-shape (left) and pre-sample (right). The boxes labelled "D" indicate the diode positions. The nominal borders of the pixels are shown by the right-angled corners and dotted lines.*

The sensitive analogue front-end circuits are located in the very centre of the pixel with extensive substrate-grounded guard rings for signal integrity. Analogue signals are routed primarily on metal layer 1, with some plates of metal layer 2 used where necessary to shield the analogue signals from switching signals passing overhead. The deep P-well layer is added as a symmetrical cross structure which leaves only the collecting N-well diodes exposed to the epitaxial layer, as shown in figure 9.

Figure 9. *Pixel deep P-well implant layouts; pre-shape (left) and pre-sample (right). The orientation is the same as in the previous figure. The nominal border of the pixel is shown by the dashed lines, so the areas outside this are part of the eight neighbouring pixels. The grey shows the deep P-well implant area while the purple shows the N-well structures. All the N-well regions are protected by deep P-well implant except for the four signal diodes towards the pixel corners.*

Pixel power supplies are routed on the metal layers 3, 4 and 6 in horizontal and vertical directions to distribute power in a mesh structure. The various sub-circuits in each pixel design are

mostly powered separately in this first sensor, so there are five independent power supplies routed to the pixels. The hit output signals from pixels are routed horizontally along a row on metal layer 5, which is fully shielded from the sensitive analogue electronics below by the metal layers in between.

2.7 Row control logic

The row logic is responsible for monitoring the individual hit outputs from a row of 42 pixels and writing details of any hits to local memory. An external clock defines the timing with which hit signals are sampled. The hit signal from a pixel is asynchronous, but will have a fixed output pulse width defined by the in-pixel monostable bias setting. This pulse length would typically be set to be around 10% greater than the hit sampling period, which would be matched to the bunch crossing rate of the target application, typically 200-400 ns. This regime ensures that an asynchronous hit will always be sampled by the synchronous logic, with a small probability that it will be sampled twice. This is an acceptable data overhead that allows for a reasonable spread in the length of the monostable pulses, with a minimal risk that an entire hit pulse occurs between sampling such that the hit is lost. The sampling of hits uses an alternating ("ping-pong") circuit architecture to ensure there is no dead time between samples.

The 42 sampled hit signals are subdivided into seven "banks" for most efficient processing and storage. Each bank is selected for inspection in turn with a three-bit multiplex (MUX) address code. An OR circuit then tests the six pixel outputs of the bank to see whether the bank contains any hits. If so, the six-bit pixel hit pattern and the three-bit MUX address code are stored, thus identifying a single location in the full row of 42 pixels. This is illustrated in figure 10. A feature of this approach is in the case of a dense particle shower, for which multiple nearby hits are stored in a single register, rather than multiple registers. The hit-seeking circuits operate at eight times the bunch crossing rate, i.e. up to 50 MHz. Multiplex signals are gray-coded for reliable high speed operation, and the reserved address value 0 deselects all banks for additional testing provision.

2.8 Data storage

The row control logic has 19 SRAM registers available for storage of hit data. A memory controller is implemented to organise the use of these registers, such that registers are not overwritten once used, and only those with valid data participate in readout. This memory controller is implemented as a bidirectional shift register, with 20 cells. The memory control register initialises with a token in the first position, which enables the first SRAM register for write access. During data write the shift register advances to the next position, filling the SRAM registers in order for the first 19 hits. A further hit in the row then moves the token into a holding cell, which raises a global overflow flag indicating the memory full status. This hit, and any further hits on that row, will be discarded.

The row control logic may be operated in "hit override" mode, whereby the result of the OR circuit is ignored and the value of the hit pattern in each bank is always stored. This operating mode fills the memories in less than three complete cycles of the standard control sequence, and so is intended as a test feature.

The 19 SRAM registers occupy the full $50\,\mu$m row pitch. The hit pattern and corresponding MUX address are stored in the first 9 bits of a register, with a further 13 bits used to store the
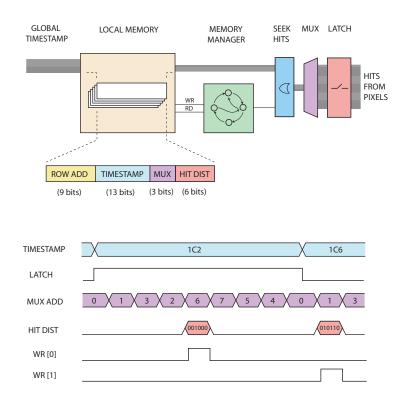
Figure 10. *Overview of the row logic for hit storage; see text for details.*

global timestamp code, which is incremented each time hit signals are sampled. The cross-coupled inverter structure of a SRAM cell ensures the data will be held indefinitely provided the cell is powered, so there is no requirement to refresh the data and no maximum hold time after which data are corrupted.

The full TPAC 1.0 sensor comprises four columns of row logic, each with 168 rows, hence there are 12,768 SRAM registers of 22 bits each in total. The row control logic and the SRAM register bank occupy a $250\,\mu$m wide region adjacent to the 42 pixels, equivalent to the area of five pixels. There is no sense circuitry in this region and, as no deep P-well is added here, charge arising from particles that pass through these regions will be collected by local N-wells associated with PMOS transistors in the logic and SRAM. This charge will not be collected as signal and the logic and SRAM are therefore insensitive to incident particles. In addition, an inactive $50\,\mu$m wide strip across the centre of the sensor corresponding to a single row of pixels, is used to distribute bias and reference voltages, and to re-buffer control signals. These inactive regions result in the sensor having an inherent 11% dead area.

2.9 Readout

During readout, the memory controller is switched into the reverse direction and clocked once to initialise the token to enable the most recently written register for readout. A combinational read-enable signal propagates to the first register that has valid data for readout, and enables the connection to the parallel readout bus. On each subsequent clock of the memory controller the next

valid register is selected until no further registers remain, at which point a "done" output flag is asserted. The off-sensor control software uses this flag to initiate readout of each logic column in turn.

In addition to the 22-bit SRAM registers, a 9-bit ROM cell is activated during readout of each row. These extra cells encode a unique row address that forms part of the parallel data bus.

The SRAM and ROM readout is implemented with a current sense amplifier which was optimised to operate over long distances with minimal read time. An activated SRAM or ROM cell pulls current from the parallel data bus depending on its state, which is sensed by the circuit at the column base. A total of 31 of these current-sense amplifiers operate in parallel to create a 31-bit digital output data word, which is multiplexed and driven off-sensor with no serialization. The maximum read time from the furthest cell is 150 ns and parallel data readout is typically operated at a 5 MHz rate. A full sensor readout, in which every register contains valid hit data (such as when operating in hit override mode) therefore takes approximately 2.6 ms, and generates 50 kBytes of data.

2.10 Pixel test structures and additional test features

In addition to the main design presented above, the TPAC 1.0 sensor has three pre-sample test pixels on the periphery which have been implemented to allow access to internal nodes for evaluation. The test pixel designs correspond to both the quadrant 2 and 3 variants but also include additional analogue buffers to monitor internal analogue signals in the pixel circuit. These facilitate evaluation of the performance of monostable circuits, comparators, trim adjustment of threshold, and the analogue front end circuits for the pre-sample pixel architecture. The signal pulse and the reset sample are available for two adjacent pixels, and the internal differential comparator output is available from one of these. A third pixel allows evaluation of other in-pixel circuits, including the two monostables and the full comparator chain. The circuit is shown in figure 11. These test pixels are included at the edge of the main pixel array. Due to a lack of time before submission, no pre-shaper test pixels were implemented. However, a pre-shaper test pixel corresponding to the quadrant 1 variant was included on TPAC 1.1, again with internal signal connections. This is also shown in figure 11.
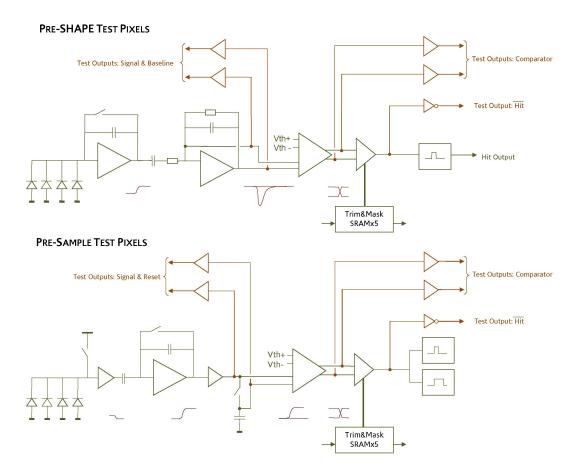
In addition, key digital signals, such as control clocks and the least significant bit of the multiplex address and time-code are driven off-sensor at the farthest point from their initial distribution. This debug feature allows the timing of critical signals to be evaluated during operation.

All bias currents are independent and are generated off-sensor to evaluate the performance of sub-circuits in different operating modes. The two pixel architectures can be operated independently, with separate threshold voltage, bias settings and power-down control.

2.11 DAQ system and operation

For all the tests described in this paper, the sensor was mounted on a custom-designed PCB and read out with a USB-based readout system using a custom software data acquisition (DAQ) system.

The PCB design was compatible with both TPAC 1.0 and 1.1 sensors. It included 31 DACs to allow all the bias voltages and currents for the sensor to be software controlled. It also held a temperature sensor. Each PCB was given a unique ID through a dip switch which could be read
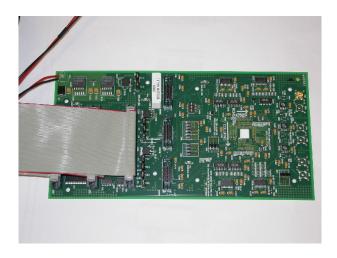
Figure 11. *Test pixel circuits for pre-shape on TPAC 1.1 (upper) and pre-sample on TPAC 1.0 (lower), showing the internal nodes which are accessible externally.*

out to the DAQ. Below each sensor, a hole approximately $8 \times 8\,\mathrm{mm}^2$ was cut in the PCB to allow access to the substrate for use with a laser (see section 5.3). An additional notch approximately $1 \times 1\,\mathrm{mm}^2$ was also cut below the test pixel structures, again to allow illumination by a laser. The PCB hole left a strip approximately 1 mm wide for gluing the sensor to the PCB. Around 20 sensors were mounted on PCBs and no mechanical failures of this glue joint were found. Conductive glue was used to allow the substrate to be optionally grounded. The sensor required 265 wirebonds to connect to the PCB. The PCB is shown in figure 12.

Three 64-way flat ribbon cables connected the sensor PCB to a generic readout board, the USB_DAQ card, which provided the USB interface to the computer. The USB_DAQ card required firmware specific to the TPAC 1.0 or 1.1 sensor to generate the required control and timing signals, as well as the configuration load and readback, and the data memory readout. It also controlled the PCB DAC settings and performed the temperature and PCB ID readout.

The sensor was operated with fake "bunch trains" to mimic ILC operation. A bunch train consists of a period of data acquisition where pixel hits are registered and timestamped according to a "bunch crossing" clock. Following a fixed number of bunch crossings, the data acquisition is halted and the pixel hits are read out. The timing structure of the bunch train was controlled by

Figure 12. *Photograph of the PCB used to hold and operate the sensor. The hole with the sensor mounted on the lower side is just right of centre.*

the USB_DAQ and was to a large extent under software control. For all following measurements, the operating parameters for the bunch train used were a 400 ns period bunch crossing clock and a number of bunch crossings up to the maximum timestamp storable in the memory of 8192.
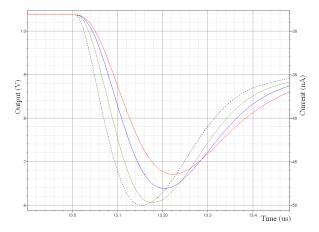
3. Pixel charge diffusion simulation

The signal from a minimum ionising particle (MIP) arises as the particle passes through the sensor. Physically, electron-hole pairs are created throughout the silicon sensor. Within (or near) the epitaxial layer the liberated electrons are able to diffuse to the collecting diodes and hence be seen as signal. Some electrons from the substrate close to the epitaxial layer can also diffuse into the epitaxial layer and so be collected. However, electrons in the deep P-well implant will mostly be lost. Overall, for a MIP at normal incidence to a sensor with a $12\,\mu$m thick epitaxial layer and deep P-well, around $1100\,e^-$ will be available to contribute to the signal. Due to diffusion from the substrate, a $5\,\mu$m thick epitaxial layer will yield around half this value. Once liberated, the charge diffuses and may be absorbed by the collection diodes of the neighbouring pixel. In addition, other N-well structures can collect charge and hence charge will be lost in terms of being signal. This last effect is the reason for which the deep P-well implant was developed.

As described in Section 4.1, for calibration, the sensor was exposed to an intense [55]Fe source. This isotope produces gamma radiation including prominent K_α lines with photon energies close to 5.9 keV. There is also a lower rate of K_β photons, with energies close to 6.5 keV. Photons of these energies can interact in the silicon, again causing ionisation, and will liberate all the signal charge within a small $O(1\,\mu m^3)$ volume. In most cases when the photons convert in the epitaxial layer, a significant fraction of the charge will diffuse out of the pixel and be absorbed in the neighbouring pixels, being lost as signal to the hit pixel. Hence only a small fraction of the signal will be collected by the diode and a spread of signal sizes will be observed, depending on the details of the charge diffusion. However, a small number of the photons will interact directly inside the signal diodes

themselves. In this case, all the charge liberated, around $1620\,e^-$, will be collected by the diode and a fixed signal size will be observed.

Another difference between an interaction in the diode and elsewhere in the epitaxial layer is the speed of charge collection. Charge deposited in the diode should be collected quickly, of the order of 1 ns, while the diffusion of charge from the epitaxial layer takes of order 100 ns. The diffusion time is convoluted with the preamplifier response and signal shaping circuit, which results in a slower rise time and lower peak for longer collection times. Figure 13 shows the simulated pre-shaper circuit response resulting from the different signal time characteristics. A diode interaction signal is found to be around 15% larger than a more general epitaxial layer interaction, for the same total charge collected.
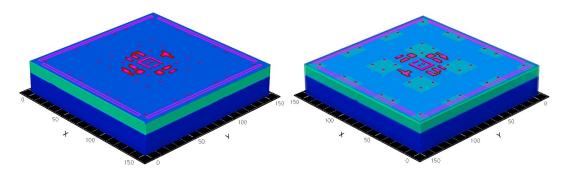

Figure 13. *Simulated reponse of pre-shape circuit to pulses of the same magnitude but with varying collection times. The pulse charge is injected at 13 µs on the time axis and collected with an exponential rise, with time constants of 0 ns (black, dashed), 25 ns (green), 50 ns (blue) and 75 ns (red). Zero corresponds to a diode interaction while a typical epitaxial interaction corresponds to the 50 or 75 ns curve.*

3.1 Detailed simulation

To estimate the signal spread quantitatively, a simulation of the sensor pixel was performed using the Sentaurus [11] package. The pixel GDS design file was used as input to the simulation, ensuring the details of the pixel were correctly simulated. Figure 14 shows the pre-sampler pixel simulated. The pre-shaper diffusion is expected to be very similar as the diodes are placed identically in the two designs; this is particularly true for the deep P-well sensors as very little charge is expected to be absorbed by the circuit N-wells. Only modelling of the diffusion of MIP signals was performed with this detailed simulation.
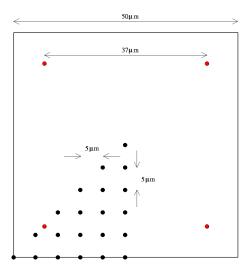
Charge equivalent to that expected for a MIP passing perpendicularly through the epitaxial layer was deposited at various locations within the pixel and then its diffusion was simulated to investigate where it was absorbed or lost. A 3×3 array of pixels was simulated to allow for neighbour pixel charge collection. The simulation assumed a 15 µm epitaxial layer and simulated the volume from the sensor surface down to 32 µm below the surface ($150 \times 150 \times 32\,\mu\text{m}^3$ in

Figure 14. *Diagram of the GDS simulated volume for the pre-sampler pixel charge diffusion modelling; without deep P-well (left) and with deep P-well (right).*

total). A correction is made for all results shown below to account for the difference between the 15 μm epitaxial thickness assumed in this simulation and the 12 μm eventually implemented in the fabricated sensor.
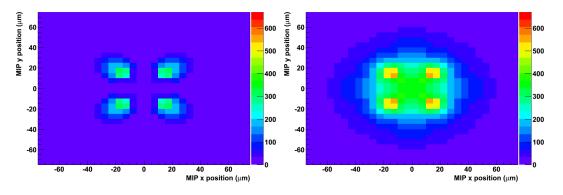
The simulation was CPU-limited so only a small number of MIP impact positions were modelled. Because of the approximate eight-fold symmetry of the sensor, all positions simulated were within a triangle with the pixel centre, corner, and side centre as its three corners. Within this triangle, the positions simulated were spaced 5 μm apart, resulting in 21 points in total. Using the approximate pixel symmetry, these could be translated and rotated to give a 5 μm regular array across the whole of the central pixel. Figure 15 shows the layout of the 21 points simulated.

Figure 15. *Layout of the 21 points (black circles) used for MIP charge deposits in the Sentaurus simulation. The red circles indicate the four diode positions.*

The simulation results are shown in figure 16 for sensors with and without the deep P-well implant. Here the fraction of the signal charge predicted in all nine pixels of the 3×3 array is shown. It is seen that the signal in all cases is predicted to be significantly larger with the deep P-well implant. In particular, in the central pixel, the fraction of charge seen depends on the position

of the incident particle. The signal varies between 20% and 50% with the deep P-well implant, with an average over the pixel of 30%. However, without the deep P-well implant, the central pixel signal can be less than 1% and only reaches a maximum of 30% when near the diode. The average for this case is less than 10%. Similar large differences are seen for the neighbouring pixels also.

Figure 16. *Sentaurus simulation of the MIP charge (in unit of e^-) seen as signal for no deep P-well (left) and deep P-well (right), as a function of the MIP impact position relative to the centre of the pixel. The simulation assumed a 15 μm thick epitaxial layer, but the values shown are scaled to those expected for a 12 μm layer.*
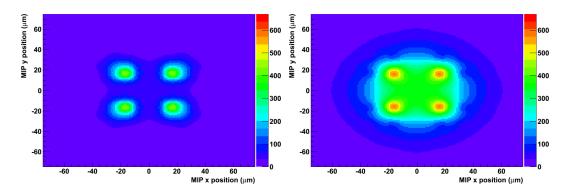
3.2 Diffusion simulation

The Sentaurus simulation was too time-consuming to model a large number of charge deposition points, so a simplified model was used for studying bigger samples of points and for modelling the ^{55}Fe calibration response. A simple diffusion equation
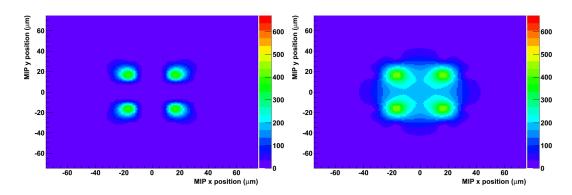
$$\frac{\partial \rho}{\partial t} = -D\nabla^2 \rho$$

was numerically solved, using an forward-time/centre-difference (FTCD) method, to model the charge density ρ within the epitaxial layer. The diffusion coefficient D, and parameters to model the charge collection with and without deep P-well implants at the surface, were adjusted to agree with the results of the Sentaurus simulation for the above 21 points. The simulation was extended to a 5×5 array of pixels and both a 5 or 12 μm epitaxial depth using a 1 μm grid. Thus a total of $250 \times 250 \times 5$ or $250 \times 250 \times 12$ volume elements were used. The MIP deposits were again simulated within the same triangle as shown in figure 15 but with 1 μm spacing, giving a total of 351 points. Figure 17 shows the equivalent distributions to figure 16 for MIP deposits resulting from the simple diffusion model, showing the much finer spacing. Only the central 3×3 pixels are shown, although the simulation volume extended beyond this region. Figure 18 shows the same but for the 5 μm epitaxial layer thickness.
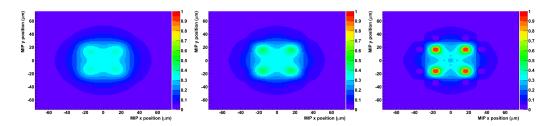
For modelling the response to the ^{55}Fe calibration photons, the charge deposits need to be simulated not only over the area of the pixel but also at various depths in the epitaxial layer. The simple diffusion model was used to estimate the spectrum of the charge collected for randomly

Figure 17. *Simple diffusion simulation of the amount of a MIP charge (in unit of e^-) seen as signal for no deep P-well (left) and deep P-well (right), as a function of the MIP impact position relative to the centre of the pixel. The epitaxial layer thickness is 12 μm in these cases.*
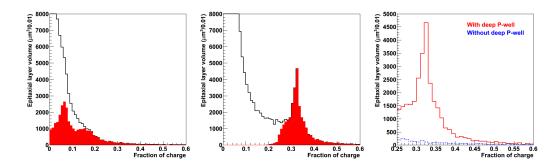

Figure 18. *Simple diffusion simulation of the amount of a MIP charge (in unit of e^-) seen as signal for (left) no deep P-well and (right) deep P-well, as a function of the MIP impact position relative to the centre of the pixel. The epitaxial layer thickness is 5 μm in these cases.*

Figure 19. *Simple diffusion simulation of the fraction of the charge seen as signal for a deep P-well pixel, as a function of the ^{55}Fe photon impact position relative to the centre of the pixel at three different depths in the epitaxial layer. Left: furthest from the diodes, centre: in the middle, right: nearest to the diodes. The epitaxial layer thickness is 12 μm in these cases.*
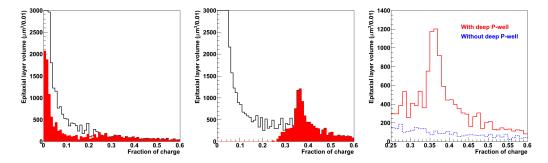
positioned charge deposits (as expected for ^{55}Fe) throughout the volume of the epitaxial layer. Examples to illustrate the depth dependence are shown in figure 19.

As can be seen in figure 19, the simulation indicates that for the deep P-well cases, there is a broad "plateau" near the centre of the pixel, effectively independent of epitaxial layer depth, where an approximately constant fraction of the deposited charge is collected. This spectrum of observed charge is shown in figures 20 and 21, which show the constant fraction is between 0.3 and 0.4, meaning that a peak corresponding to around 30-40% of the ^{55}Fe energy would be observed. This fraction is only weakly dependent on epitaxial layer depth. (Note, the full energy peak resulting from hits within the signal diodes is not due to diffusion and so is not seen with this simple model.) For pixels with no deep P-well, then no such plateau peak is seen in the simulation, so it is expected that only the full energy peak should be visible in this case. Also, for no deep P-well, the absolute rate of photons with a significant fraction of the full energy is expected to be significantly lower.

Figure 20. *Simple diffusion simulation of the fraction of the ^{55}Fe charge seen as signal for a uniform distribution of photon hit positions throughout the epitaxial volume for no deep P-well (left) and deep P-well (centre). The y-axis represents the epitaxial layer interaction volume of a pixel which results in the given signal fraction. The filled red histogram shows the fraction of signal charge absorbed in the central pixel, while the white histogram shows the spectrum of charge absorbed by the centre pixel as well as the eight neighbouring pixels. Right: overlaid comparison of the total distributions from the left and centre plots for simulated deep P-well (solid, red) and non-deep P-well (dashed, blue) spectra for an equal irradiation exposure. The epitaxial layer thickness is 12 μm in these cases.*

The volume for photon interactions which give the plateau constant value for the deep P-well case is a significant fraction of the epitaxial volume. For a 12 μm epitaxial layer thickness, it is estimated from the simulation to be around 30% of the $50 \times 50 \times 12\,\mu m^3$ pixel volume, i.e. around $10,000\,\mu m^3$. For the 5 μm epitaxial layer thickness case, it is around 25%, i.e. $3000\,\mu m^3$. The volume within the diodes which would give a signal corresponding to the total ^{55}Fe energy is estimated to be approximately a circle of diameter 5 μm and depth 1 μm, giving a total volume for the four diodes of around $100\,\mu m^3$. This is independent of epitaxial layer thickness. Hence, the plateau region is expected to be much larger, by around two orders of magnitude, than the diodes for a 12 μm epitaxial layer depth and somewhat smaller for a 5 μm epitaxial layer depth. Therefore, two peaks are expected from the ^{55}Fe exposure; a large one around 0.3 of the photon energy and a much smaller one at the full photon energy.

Figure 21. *Simple diffusion simulation of the fraction of the ^{55}Fe charge seen as signal for a uniform distribution of photon hit positions throughout the epitaxial volume for no deep P-well (left) and deep P-well (centre). The y-axis represents the epitaxial layer interaction volume of a pixel which results in the given signal fraction. The red histogram shows the fraction of signal charge absorbed in the central pixel, while the white histogram shows the spectrum of charge absorbed by the centre pixel as well as the eight neighbouring pixels. Right: overlaid comparison of the total distributions from the left and centre plots for simulated deep P-well (solid, red) and non-deep P-well (dashed, blue) spectra for an equal irradiation exposure. The epitaxial layer thickness is 5 μm in these cases.*
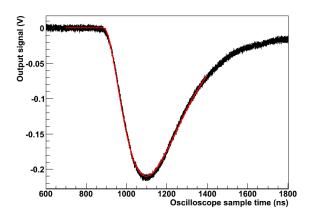
4. Test pixel performance

4.1 Test pixel performance and calibration

As described in section 2.10, the sensors included test pixels outside the 168×168 "bulk" pixel array. Several internal nodes of these pixels are accessible externally, allowing analogue measurements of their levels.
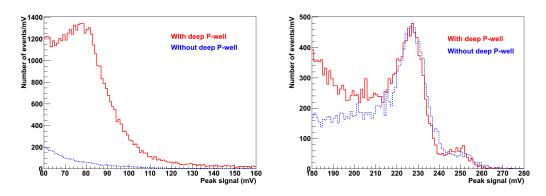
A low noise pre-amplifier was connected to the output node from the shaper, the "Test Output Signal" shown in figure 11 for the pre-shaper on TPAC 1.1, and the signals were measured on a digital oscilloscope with a 5 GHz sampling rate. This system was used to measure the peak signal seen when the test pixels were exposed to the ^{55}Fe source. A powerful GBq source allowed a sufficient rate of source hits that a calibration signal could be seen in the individual test pixels. Two different oscilloscope trigger threshold levels, 30 and 120 mV, allowed the plateau and full energy peaks, respectively, to be measured separately. An exponential rise was convoluted with the pixel circuit response (the pre-amplifier and CR-RC shaper) and the resulting functional form fitted to the oscilloscope data to extract the peak magnitude, the exponential rise time and the start time of the signal for each trigger. A typical oscilloscope output and the resulting fit are shown in figure 22.

The spectra of the magnitude of the fitted peak signals observed in 12 μm epitaxial layer sensors are shown in figures 23. and 24. The full energy peaks are similar with or without deep P-well as these mainly result from photon interactions in the diode, where there is no deep P-well implant. Comparing the plateau peaks to the simulation, the data spectra correspond roughly to an equivalent charge fraction as shown in figure 20, and 21. For the 12 μm epitaxial thickness case, it is seen that the plateau peak position and the relative rates for deep P-well and no deep P-well are in reasonable agreement, although the plateau peak width is clearly much broader in the data. Given
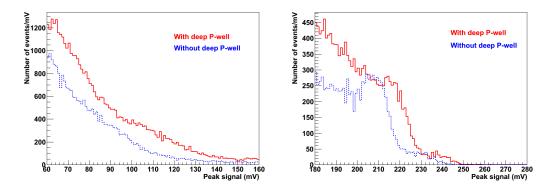
Figure 22. *Typical deep P-well test pixel oscilloscope signal when exposed to ^{55}Fe photons. The solid red line shows the result of the fit performed to extract the peak and time constants of the signal.*

the simple level of simulation used, this is not unreasonable. For the $5\,\mu$m epitaxial thickness case, there is no clear peak; the absence of the peak predicted by the simulation is not understood.

Figure 23. *Test pixel peak signal spectra when exposed to ^{55}Fe photons for deep P-well (solid, red) and non-deep P-well (dashed, blue) sensors. Left: peaks of ^{55}Fe signal around plateau energy, normalised to equivalent exposures. Right: peaks of ^{55}Fe signal around full energy; the prominent peaks around 225 mV are from K_α photons of energy 5.9 keV, while the smaller peaks around 250 mV are due to K_β photons of energy 6.5 keV. These spectra are from sensors with a $12\,\mu$m thick epitaxial layer.*
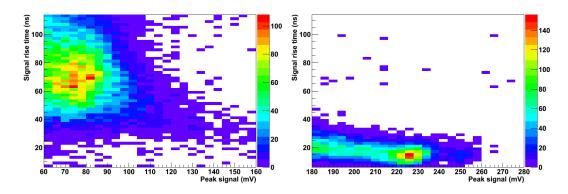
The noise measured by the oscilloscope is $3\,$mV. Both this noise and the full energy peak positions are consistent both with and without deep P-well, showing the deep P-well implant does not affect the circuit performance. For the deep P-well, $12\,\mu$m epitaxial thickness, the full peak corresponds to $1620\,e^-$ charge, so the noise is equivalent to $22\,e^-$. Allowing for a gain of 0.8 in the external low-noise preamplifier, the pre-shaper gain is measured to be $160\,\mu$V$/e^-$. These values are completely consistent with the expectations given in section 2.3. In addition, the ratio of the plateau to full peaks is 34% which is in reasonable agreement with the simple diffusion simulation, see figure 20. Given the approximations used in this model, the agreement is regarded as sufficient

Figure 24. *Test pixel peak signal spectra when exposed to* ^{55} *Fe photons for deep P-well (solid, red) and non-deep P-well (dashed, blue) sensors. Left: peaks of* ^{55} *Fe signal around plateau energy, normalised to equivalent exposures. Right: peaks of* ^{55} *Fe signal around full energy; the peaks around 215 mV are from* K_α *photons of energy 5.9 keV, while the smaller peaks around 235 mV are due to* K_β *photons of energy 6.5 keV. These spectra are from sensors with a 5 μm thick epitaxial layer.*

to be confident that the source of these peaks is understood.

As a final check of the origin of these peaks, figure 25 shows the correlation of the fitted exponential rise time constants of the signals as a function of the fitted peak signal magnitude. The full peak values have rise times of around 10 ns while the deposits resulting in the plateau peak have a rise time of around 70 ns. The strong correlation shows the highest peak values, which correspond to the diode interactions, have the shortest time constant, as expected, while the plateau signal, from lower in the epitaxial layer, has a slow collection time; see section 3.

Figure 25. *Deep P-well test pixel signals when exposed to* ^{55} *Fe photons, showing the number of events (indicated by the colour scale) seen as a function of the signal peak value and exponential time constant, both extracted from a fit. Left: the plateau region. Right: the full peak region. These data are from a sensor with a 12 μm deep epitaxial layer.*

5. Bulk single pixel performance

5.1 Pedestals and noise

The performance in the bulk pixels is less straightforward to measure as there is no analogue read-out available. However, the rate of hits in each pixel as a function of the applied threshold effectively allows the integral of the analogue spectrum to be measured and hence the spectrum itself can be estimated. The results in this section are based on performing such "threshold scans" and measuring the response.

One further complication is that pickup was observed between pixels when O(100) were enabled and firing at the same time (see section 6.2). This is not a major problem when operating the sensor for its design purpose as only O(10) pixels per sensor are expected to fire in each event. However, for the basic performance measurements presented below, this pickup could prevent the response of individual pixels from being measured. Hence to remove this sensor-wide effect, only a small number of pixels are unmasked at any time for the following results.

Specifically, only one pixel of the 42 which shared SRAM memory was unmasked in each run. In addition, runs were performed with only 19 bunch crossings per bunch train. Both of these together ensured that the memory could never overflow and so distort the threshold scan, even when very close to threshold.

The pixel comparator only fires when the input crosses through the threshold from below. Hence, a threshold scan performed with no external stimulus will result in hits only when near the pixel pedestal. The results of such a scan for a typical pixel are shown in figure 26. Here, the scan is specified in the (arbitrary) units of the DAC threshold setting, called "DAC threshold units" (DTU) in this paper.
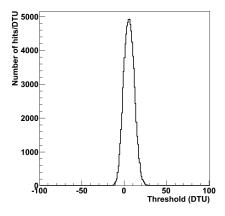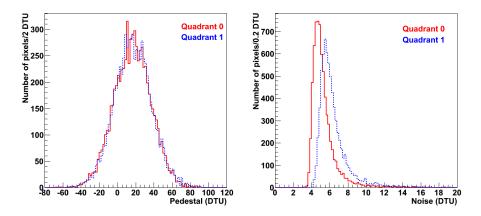

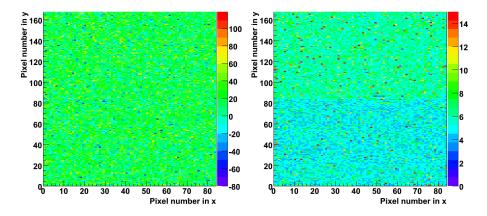**Figure 26.** *Typical pixel threshold scan for a pre-shape pixel.*

For the pre-shape threshold scan, the resulting distribution is well described by a Gaussian and so can be characterised by the mean and the RMS. The mean gives the pedestal for the pixel and the RMS gives the noise [12]. The distribution of the pixel mean and RMS values for the two pre-shape quadrants (see Section 2.3) of a typical sensor are shown in figure 27. It is seen that there is a significant spread of pedestals within a quadrant. The pedestal spread RMS is around 20 DTU

and is the same for quadrants 0 and 1. This is much bigger than the noise on the pixels, which has an average value of around 5 DTU for quadrant 0 and 6 DTU for quadrant 1.

Figure 27. *Distributions of pedestals (left) and noise (right) for pixels in quadrants 0 (solid, red) and 1 (dashed, blue), in DAC threshold units (DTU), for a typical sensor. Pixels in these two quadrants are all of the pre-shape design. All trim values were set to zero.*
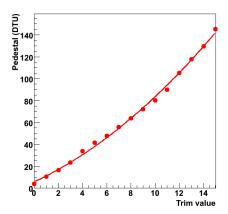
The values of the pedestal and noise for each pre-shape pixel of a typical sensor as a function of the position within the sensor are shown in figure 28, where the difference in noise for the two quadrants is visible. The values of the pedestals and noise show no correlation with position within each quadrant and their spreads appear genuinely random pixel-to-pixel. There is no correlation between the pedestal and noise values.

Figure 28. *Two-dimensional map of pedestals (left) and noise (right) for the two pre-shape quadrants of a typical sensor. The lower half of each plot corresponds to quadrant 0 and the upper half to quadrant 1. The colour-coded scale is in DAC threshold units (DTU) in both cases.*

The spread of pedestals can be reduced using the per-pixel trim setting. This allows a value in the range 0-15 to be loaded to each pixel to adjust the pedestal position upwards. The effect of this

on the pedestal of a typical pixel is shown in figure 29. It is seen that there is a non-linear effect in the response.
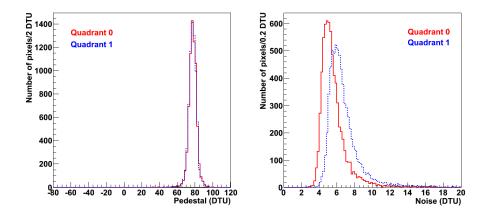

Figure 29. *Change of pedestal for a typical pixel as a function of the trim setting. The curve shows a second-order polynomial fit to the data points, illustrating the response is non-linear.*

The spreads of pedestals after trimming a typical sensor are shown in figure 30. It is seen that the RMS of the pedestals is reduced by a factor of around five. The resulting spread is a little smaller than the size of the per-pixel noise and so gives a small but non-negligible contribution to the apparent noise rate when setting a common threshold for all pixels. The ability to improve on this effect is limited by the number of trim bits available. With four bits, then a granularity of the trim of 16 values is possible. However, the total range of the uncorrected pedestals is around 100 DTU, so that even with careful matching of the trim range, the trim least significant bit would be around 6 DTU. Two additional trim bits have been implemented in the next version of the sensor. The average noise is unaffected by trimming, although the spread of the noise is slightly increased.
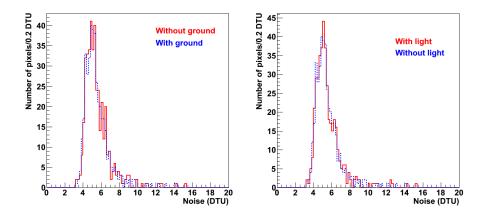
We investigated the pixel noise under a variety of external factors. The sensor substrate can be grounded or operated with no explicit bias connection to the substrate. This could in principle change any environmental noise pickup. The distribution of noise for a subset of pixels both with and without the substrate being grounded are shown in figure 31. It is seen that leaving the substrate unconnected has no significant effect on the noise. In addition, the sensor may be sensitive to light and it is normally operated with a cover to keep it in the dark. However, the six metal layers used effectively completely cover the top surface of the sensor so little light reaches the epitaxial layer. Figure 31 also shows the noise distribution of the same pixels with and without a strong lamp being shone on the top surface of the sensor. Again, there is no significant difference.

5.2 Bulk pixel calibration

The calibration of the threshold setting in DTU to a physical scale was performed using an ^{55}Fe source using the same principle as described in section 4.1. The same high-rate source was used, giving a sufficient rate of hits to calibrate individual pixels. A threshold scan was performed and the rate plotted as a function of the threshold setting. A numerical derivative was then taken of this

Figure 30. *Distributions of pedestals (left) and noise (right) for pixels in quadrants 0 (solid, red) and 1 (dashed, blue), in DAC threshold units (DTU), for a typical sensor, following the determination of the optimal trim values.*
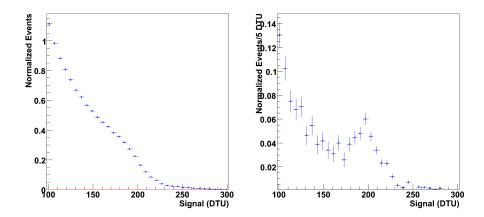

Figure 31. *Left: noise distribution with (dashed, blue) and without (solid, red) grounding the substrate. Right: noise distribution with (solid, red) and without (dashed, blue) a strong light source shining on the sensor.*
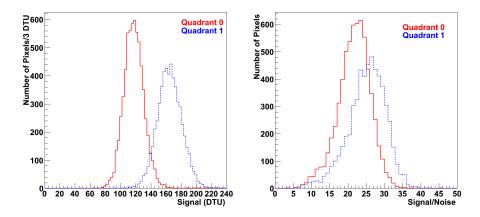
rate plot to get the basic spectrum and so to find the calibration peak. The results for a typical pixel are shown in figure 32. The observed peak corresponds to the plateau peak, as the full energy peak is above the operating range of the comparator.

The peak positions (corrected for pedestal) for the pre-shape pixels measured in both quadrants 0 and 1 are shown in figure 33. The average signal for quadrant 1, 165 DTU, is significantly higher than for quadrant 0, 117 DTU, by around 35%, while the spreads of the signals for quadrants 0 and 1 are 11% and 10%, respectively. As shown above in figure 27, quadrant 1 also has a higher average noise than quadrant 0, by around 20%, so quadrant 1 has a better signal/noise ratio (averaging 25 compared with 22), also shown explicitly in figure 33.

The variations in the position and width of the peak measured are shown as a function of

Figure 32. *Left: rate of hits as a function of the threshold setting. Right: numerical derivative of the rate plot. The ^{55}Fe calibration signal is visible at around 190 DTU, as a shoulder in the left plot but as a clear peak in the right plot. The epitaxial layer thickness is 12 μm in this case.*
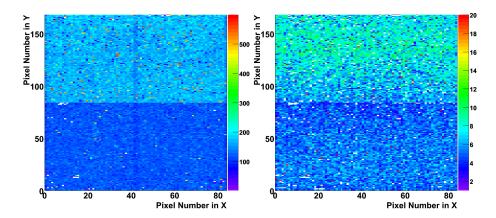

Figure 33. *Distribution of ^{55}Fe signal peak position (left) and signal/noise (right) for pixels in quadrants 0 (solid, red) and 1 (dashed, blue).*

the position in the sensor in figure 34. The differences of the two quadrants are clearly visible. However, within the quadrants, similarly to figure 28, there is no correlation between the gain or noise and the position in the sensor.

For quadrant 0, the average peak position relative to the pedestal was found to be 117 DTU. From section 4.1, this corresponds to 34% of the of the $1620\,e^-$ of signal charge, i.e. $550\,e^-$, so this calibrates 1 DTU to be $4.7\,e^-$. For quadrant 1, then 1 DTU is equivalent to $3.3\,e^-$. This can be used to interpret the noise measurements above. The average noise values of 5 DTU and 6 DTU, for quadrants 0 and 1 respectively, correspond to an equivalent in terms of signal charge of $23\,e^-$ and $20\,e^-$. Hence, the measured bulk pixel noise is compatible with both the test pixel measurements and the predicted design value.

In terms of detection of MIP signals, then the typical signal in the pixel hit by a charged
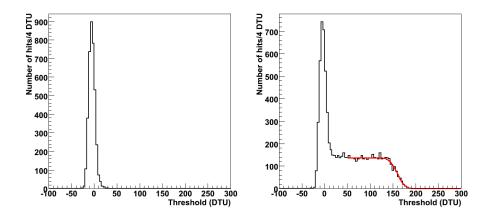
Figure 34. *Two-dimensional map of ^{55}Fe peak position (left) and peak width (right) for the two pre-shape quadrants of a typical sensor. The lower half of each plot corresponds to quadrant 0 and the upper half to quadrant 1. The colour-coded scale is in DAC threshold units (DTU) in both cases. Pixels for which no peak was measured are shown as white. The faint vertical line in the centre of the left plot corresponds to the pixels bordering the dead area between the two readout regions, which has no deep P-well implant.*

particle is the plateau fraction of around 30% of the $1100\,e^-$ deposited, i.e. $350\,e^-$. Hence, this corresponds to an expected typical signal/noise ratio for MIPs of around 15.
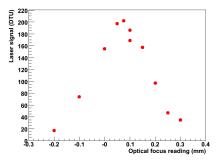
5.3 Bulk laser signal response

The sensor was illuminated using a laser of wavelength 1064 nm. The laser enclosure contained a computer-controlled moveable XY stage, on which the sensor PCB could be mounted. This allowed the sensor to be moved in two dimensions below the laser, allowing a large number of measurements which are described in this section. For these measurements, the signal was injected into the bulk pixel area and the response measured using a threshold scan. A typical response is shown in figure 35, where the laser signal is clearly seen. The actual size of the laser signal was found by fitting the falling edge of the response curve to an integrated Gaussian (an error function). In terms of the integrated Gaussian parameters, this gives a pseudo-analogue signal response estimate from the mean and an estimate of the signal spread from the width. The absolute intensity of the laser was uncalibrated so the signal size for the following measurements is arbitrary, although it is similar to that expected for a MIP.

The laser must be focussed onto the epitaxial layer. This was done by focussing the microscope optically on the substrate surface and then recording the observed laser signal size at various focus depths relative to this. Figure 36 shows the results of such a scan, where there is seen to be a strong dependence on the focus depth. The maximum signal was found to be $60\,\mu$m into the substrate relative to the optical focus. In addition, there is a range of only around $\pm 20\,\mu$m where the signal size is effectively unchanged. This sets a limit on the degree of tilt acceptable when performing such laser measurements. A focus on pixels near one edge of the sensor will only be within this tolerance for pixels near the other edge if the sensor is flat to around 2 mrad. For this reason, the focus was checked when large movements were made and, when possible, only small movements

Figure 35. *Typical threshold scan without (left) and with (right) the laser powered on. The right plot also shows the fit to the error function (red line), from which the laser signal was determined to be 160 DTU in this example.*

were then performed around this point.

Figure 36. *Laser signal size as a function of the focus depth relative to the optical focus position. A positive value means the focus position was moved into the sensor.*

The laser system was used to determine the relative gain of the pixels. By firing the laser into the centre of each pixel in turn, then the signal size for each was determined. Figure 37 shows the distribution of the observed laser signals and signal/noise ratios for a subset of pixels in the two pre-shape quadrants. Comparison with figure 33 shows these results are consistent with those from the ^{55}Fe measurements. Again a clear difference in both signal size (90 DTU and 130 DTU, respectively) and signal/noise (18.4 and 20.6, respectively) for quadrants 0 and 1 was observed, with quadrant 1 being higher in both cases. The signal size (i.e. gain) spread for quadrants 0 and 1 was found to be 12% and 14% respectively, which are slightly higher than, but consistent with, the ^{55}Fe measurements. Because of the better signal/noise performance, only the quadrant 1 variant of the pre-shape pixels was implemented in the next version of the sensor.

The laser system was also used to measure the charge diffusion so as to compare with the simulation described in section 3.1. The laser was focussed to give a illuminated spot size of
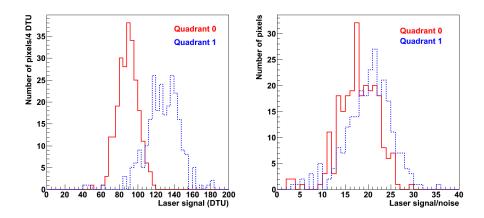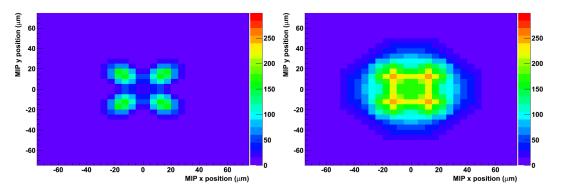
Figure 37. *Laser signal (left) and signal/noise (right) for quadrants 0 (solid, red) and 1 (dashed, blue).*

less than $2\,\mu$m and the stage could be moved with a $1\,\mu$m precision, so that the charge could be generated accurately to match the positions of the 21 points shown in figure 15. Because the laser was uncalibrated, the absolute fraction of the laser signal observed could not be determined, so only the relative shape as a function of position is relevant. Figure 38 shows the results of these measurements using sensors with and without deep P-well implants. Both sensors measured had a $12\,\mu$m epitaxial layer thickness. Bearing in mind that the simulation (shown in figure 16) does not include the effects of the laser spot size or electronics noise, it is seen that the general trend of the data is in quantitative agreement with the simulation and that the deep P-well increases the signal size significantly. Overall, it is clear that the sensor without deep P-well implants gives a much smaller signal.

Figure 38. *Charge seen as signal (in units of DTU) from laser for no deep P-well (left) and deep P-well (right), as a function of the laser impact position relative to the centre of the pixel. These data are from a sensor with a $12\,\mu$m thick epitaxial layer.*
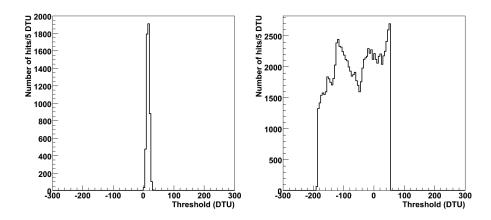
6. Global sensor performance

Global aspects of the sensor performance were also studied and are discussed below.

6.1 Configuration load

The per-pixel five-bit configuration data were loaded and read back to check for bit errors. Each load transfered 141 kbits into the sensor configuration registers. The load and readback cycle was repeated 25,000 times and the data written and readback were compared. No bits were seen to have been corrupted in this process. This sets an upper limit on the bit error rate of 1×10^{-9} at 90% confidence level.
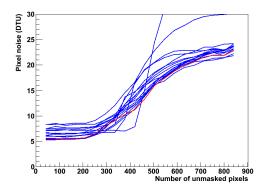
6.2 Pickup between pixels

As mentioned in section 5.1, pickup was observed between pixels when large numbers fired at the same time. For this reason, all the results described in section 5 were done with only a small number of unmasked pixels. Typical pickup behaviour is illustrated in figure 39 where the threshold scan for a single pixel is shown with just that pixel unmasked and also with all pixels unmasked. It is clear the distribution when all pixels are enabled is uncorrelated with the pedestal of the actual pixel being studied; it depends on the pedestals of the other pixels firing. The scan with pickup has a much larger RMS and this has been used to characterise the onset of pickup.

Figure 39. *Effect of pickup on a typical pixel with only the pixel enabled (left) and with all other pixels enabled (right).*

Many studies to analyse this effect were performed. It was found that the level of pickup depended on the number of pixels unmasked but not their geometric positions relative to each other. One example of these studies which shows this result clearly is shown in figure 40. In this study, a single pixel on one edge of the sensor was unmasked. The RMS of this pixel from a threshold scan was then determined as an increasing number of pixels were unmasked along the other edge of the sensor, i.e. at the furthest point from the single pixel. It is seen that pickup on the isolated pixel has the same behaviour as that of all the pixels along the far edge. Hence, the pickup is seen to be unrelated to position.

Figure 40. *Onset of pickup, as measured by the RMS determined from a threshold scan, as a function of the number of unmasked channels. Each of the 16 lines corresponds to a single pixel, one of which (in red) is on the opposite side of the sensor to the others. It is seen that pickup starts on most pixels when around 300 pixels are unmasked and it is independent of the pixel position.*

The pickup is not due to coupling directly between monostables as this would not be affected by masking pixels. It is thought that the pickup is caused by a power mesh being shared between the pre-shape comparator and monostable components. If a large number of pixels fire and give hits in the monostables, the common power level droops and causes the comparators in other pixels to fire. The power meshes to these two components have been separated in the next version of the sensor.

It is important to note that this power coupling effect does not affect normal operation of the sensor. It is only when doing sensor tests involving threshold scans with low thresholds, such as a pedestal determination, that large numbers of pixels fire simultaneously. When operating as a particle detector, then the threshold setting is high enough that only small numbers of pixels fire and hence the power droop is never large enough to cause spurious hits. In this mode, all pixels can be operated unmasked and the sensor has high efficiency.

6.3 Hit corruption

The "hit override" mode described in section 2.8 allows hit data to be stored in the sensor memory without requiring any pixels to be above threshold. In this mode, all seven banks of pixels in each row of 42 pixels will store data for every timestamp and hence the 19 data registers will be filled within the first three timestamps.

This test mode results in predictable values for the MUX address, timestamp and row address for every data word stored. These can be compared with the values read out to check for corruption. (Note, the six-bit hit data themselves are not predictable as noise can cause them to be randomly set.) A low level of corruption, at around 0.1%, was seen for the MUX address and timestamp bits, although the actual rate varied from sensor to sensor. This was traced to a design fault; the signal to write to the SRAM did not have a wide enough voltage range to guarantee the value would be written correctly. The rate of corruption was eliminated by applying an external voltage level of 2.7 V to increase the range and this was used for all the results shown in this paper. This design fault has been corrected in the next version of the sensor.

7. Conclusions

We have produced a test CMOS sensor which demonstrates much of the basic functionality required for a binary ECAL. Test results show one of the two pixel designs functions close to the expected level. Gain and noise values from both test and bulk pixels are very similar to those predicted by the design simulation. Also, the signal charge spread between pixels is close to expectations from the pixel simulation. As part of the sensor development, we worked with the CMOS foundry to develop the INMAPS process, which enables us to use a deep P-well implant to shield the signal charge from the active PMOS circuit elements. Measurements show this improves the signal collection by a factor of more than three, without affecting the gain or noise. This implant makes the sensor viable.

This work will continue with a new sensor, TPAC 1.2, which has been designed and fabricated. The new sensor contains only the pre-shape quadrant 1 pixel design, which was shown to have the better signal-to-noise ratio, modified to have the trim range extended from four to six bits. It also implements several fixes, such as the decoupling of the comparator and monostable power meshes and correcting the SRAM memory write corruption. Small adjustments have been made to the pixel layout to improve the pixel uniformity for noise and gain. This sensor is the same size as TPAC 1.0 and 1.1 and has the same number of pixels. It is I/O compatible and so can use the same sensor PCB and DAQ system. Results from the new sensor are expected to be reported in the near future.

Acknowledgments

References

[1] J. A. Ballin *et al.*, *A MAPS-based Digital Electromagnetic Calorimeter for the ILC*, Proceedings of 2007 International Linear Collider Workshop (LCWS07 and ILC07), Hamburg, Germany (2007), arXiv:0709.1346.

[2] J. Brau, Y. Okada and N. Walker (eds.), *International Linear Collider Reference Design Report*, (2007), `http://www.linearcollider.org/rdr`.

[3] CALICE Collaboration, `https://twiki.cern.ch/twiki/bin/view/CALICE/WebHome`.

[4] S. Mendis, S. E. Kemeny and E. R. Fossum, *CMOS active pixel image sensor*, *IEEE Trans. Electron Devices*, **41** (1994) 452; E. R. Fossum, *Active Pixel Sensors – Are CCDs Dinosaurs?*, *CCDs and Optical Sensors III, Proc. SPIE* **1900** (1993) 2.

[5] R. Turchetta *et al.*, *A monolithic active pixel sensor for charged particle tracking and imaging using standard VLSI CMOS technology*, *Nucl. Inst. Meth.* **A458** (2001) 677; G. Deptuch *et al.*, *Simulation and measurements of charge collection in monolithic active pixel sensors*, *Nucl. Inst. Meth.* **A465** (2001) 92.

[6] J. A. Ballin *et al.*, *Monolithic Active Pixel Sensors (MAPS) in a quadruple well technology for nearly 100% fill factor and full CMOS pixels*, *Sensors* **8** (2008) 5336.

[7] Mentor Graphics Eldo Integrated Circuit Simulation,
http://www.mentor.com/products/ic_nanometer_design/
analog-mixed-signal-verification/eldo/

[8] Cadence Virtuoso Spectre Circuit Simulator,
http://www.cadence.com/products/cic/spectre_circuit/pages/default.aspx

[9] SiD Detector Concept, http://SiliconDetector.org/.

[10] ILD Detector Concept, http://www.ilcild.org/.

[11] Sentaurus TCAD Process and Device Simulation Tools,
http://www.synopsys.com/products/tcad/tcad.html.

[12] A. Papoulis and S. U. Pallai, *Probability, Random Variables and Stochastic Processes*, Section 11.4,
4th edition, McGraw Hill, 2002.